Tuning the Kondo effect in Yb(Fe$_{1-x}$Co$_x$)$_2$Zn$_{20}$

Tai Kong, Valentin Taufour,[*] Sergey L. Bud'ko, and Paul C. Canfield

Ames Laboratory, U.S. Department of Energy, and Department of Physics and Astronomy, Iowa State University, Ames, Iowa 50011, USA

We study the evolution of the Kondo effect in heavy fermion compounds, Yb(Fe$_{1-x}$Co$_x$)$_2$Zn$_{20}$ ($0 \leqslant x \leqslant 1$), by means of temperature-dependent electric resistivity and specific heat. The ground state of YbFe$_2$Zn$_{20}$ can be well described by a Kondo model with degeneracy $N = 8$ and a $T_K \sim 30$ K. The ground state of YbCo$_2$Zn$_{20}$ is close to a Kondo state with degeneracy $N = 2$ and a much lower $T_K \sim 2$ K, even though the total crystalline electric field (CEF) splittings are similar for YbFe$_2$Zn$_{20}$ and YbCo$_2$Zn$_{20}$. Upon Co substitution, the coherence temperature of YbFe$_2$Zn$_{20}$ is suppressed, accompanied by an emerging Schottky-like feature in specific heat associated with the thermal depopulation of CEF levels upon cooling. For $0.4 \lesssim x \lesssim 0.9$, the ground state remains roughly the same, which can be qualitatively understood by Kondo effect in the presence of CEF splitting. There is no clear indication of Kondo coherence in resistivity data down to 500 mK within this substitution range. The coherence reappears at around $x \gtrsim 0.9$ and the coherence temperature increases with higher Co concentration levels.

I. INTRODUCTION

The RTM_2Zn$_{20}$ (R = rare-earth elements; TM = transition metals) series of compounds was discovered two decades ago, in 1997 [1]. The compounds crystallize in a cubic CeCr$_2$Al$_{20}$-type structure (space group $Fd\bar{3}m$) where R ions occupy a single crystallographic site. The nearest and next-nearest neighbors of R ions are all Zn and thus varying the transition metal does not significantly alter the local environment of the R^{3+}. Even though more than 85% of the atomic constituents are zinc, these compounds exhibit myriad physical properties depending on the rare earth and transition metal that are involved [2–6]. When the rare-earth element is Yb, there are six closely related YbTM_2Zn$_{20}$ heavy fermion compounds for TM = Fe, Ru, Os, Co, Rh, Ir [6,7]. Among these six compounds, YbCo$_2$Zn$_{20}$ has the largest Sommerfeld coefficient, $\gamma \sim 7900$ mJ/mol K^2. This value is comparable to the record holding YbBiPt [8], and is more than an order of magnitude larger than the other members in this family, which have γ values ranging from 520 mJ/mol K^2 for YbFe$_2$Zn$_{20}$ to 740 mJ/mol K^2 for YbRh$_2$Zn$_{20}$ [6]. The reason behind the dramatic difference between YbCo$_2$Zn$_{20}$ and the other five YbTM_2Zn$_{20}$ compounds is still not clear, although band-structure calculations reveal that the $4f$ level is closer to the Fermi level in YbCo$_2$Zn$_{20}$ than in YbFe$_2$Zn$_{20}$. Upon Co substitution, the d band is gradually filled, which is accompanied by a drop in d-band energy [9].

Having the largest γ value among all the YbTM_2Zn$_{20}$ compounds, YbCo$_2$Zn$_{20}$ has been studied intensively ever since its discovery [6]. Upon application of pressure, there is an indication that the heavy Fermi-liquid regime can be suppressed, followed by the appearance of an antiferromagnetic ordering for $P > 1$ GPa [10]. It has, therefore, been argued that YbCo$_2$Zn$_{20}$ is close to a quantum critical point (QCP) [10,11]. Similar suppressions of the Fermi-liquid regime under pressure were also observed for TM = Fe/Rh/Ir [12–14]. In the case of YbFe$_2$Zn$_{20}$, $\gamma = 520$ mJ/mol K^2 and is thus likely to be further away from a QCP in terms of the Doniach diagram; indeed, a

much higher critical pressure, around 10 GPa, was proposed in order to reach a QCP [12]. With an effective negative pressure induced by Cd substitution, the hybridization between Yb^{3+} $4f$ electrons in YbFe$_2$Zn$_{20}$ and the conduction electrons becomes weaker [15]. Apart from pressure induced ordering, metamagnetic transitions were reported for YbCo$_2$Zn$_{20}$ at high magnetic fields [16–19]. Crystalline electric field (CEF) schemes for YbCo$_2$Zn$_{20}$ have been proposed based on specific heat and anisotropic magnetization measurements. The first and the second excited CEF levels are around 10 and 25 K above the ground-state doublet [20,21]. Inelastic neutron-scattering measurements show some excitations that might be related to these proposed CEF schemes [22]. Experimentally, band structure had only been reported for YbCo$_2$Zn$_{20}$ via quantum oscillations [23], with a heavy ground state being strongly suppressed by increasing field. In a zero-field limit, the mass of the quasiparticles was extrapolated to be 100–500 times the free-electron mass.

Given that (i) the first- and second-nearest neighbors of Yb^{3+} in YbTM_2Zn$_{20}$ do not have TM and (ii) as TM changes from Fe to Co the values of T_K and γ change by an order of magnitude, it is of interest to see how the strongly correlated electron state evolves in Yb(Fe$_{1-x}$Co$_x$)$_2$Zn$_{20}$ for $0 \leqslant x \leqslant 1$. In this paper, we report the temperature-dependent resistivity and specific heat data on 19 members of the Yb(Fe$_{1-x}$Co$_x$)$_2$Zn$_{20}$ series and track the effects of band filling and disorder on the coherence and Kondo temperatures as well as amounts of entropy removed by thermal depopulation of CEF levels versus Kondo state.

II. EXPERIMENTAL METHODS

Single crystals were grown using a high-temperature solution growth technique [2,6]. The starting molar stoichiometry was Yb:TM:Zn = 2:4:94. Bulk elemental material [Yb from Ames Laboratory Material Preparation Center (99.9% absolute purity); Fe (99.98%), Co (99.9+%), and Zn (99.999%) from Alfa Aesar] was packed in a frit-disc crucible set [24] and sealed in a silica tube under $\sim$0.25 bar of Ar atmosphere. The ampoule assembly was then heated up to 900°C over 3 h; dwelt at 900°C for 10 h, and then cooled to 600°C over 100 h. At 600°C, the remaining Zn rich solution was

---

*Current address: Department of Physics, University of California Davis, Davis, CA 95616, USA.
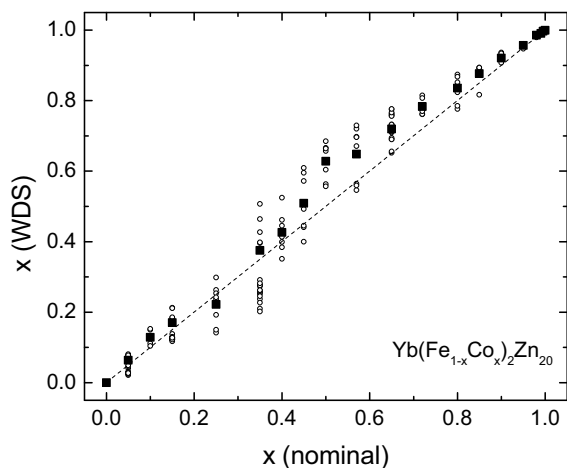
FIG. 1. Co concentrations determined by WDS as a function of nominal Co concentration values. Solid squares represent averaged WDS values. Hollow circle data points show measured values at different spots of samples. The dashed line is a guide for the eyes with a slope of 1.

decanted from the crystals that formed on cooling. Samples were cut and polished so that magnetic field is applied along the [111] crystallographic direction. Resistivity was measured using a standard four-probe technique in a Quantum Design (QD) Physical Property Measurement System (PPMS). Epotek-H20E silver epoxy was used to attach Pt wires onto the samples. Specific heat was measured using a QD PPMS. A dilution refrigerator option or a ^{3}He option was utilized to perform measurements down to 50 or 500 mK. Elemental analysis was performed via wavelength dispersive spectroscopy (WDS) using an electron probe microanalyzer of a JEOL JXA-8200 electron microprobe.

III. EXPERIMENTAL RESULTS

Figure 1 shows the WDS determined Co concentration as a function of nominal Co concentration. Although the average

value of the WDS determined concentration changes close to linearly with the nominal concentration, in the middle of the substitution range, the variation of the substitution level is large. The variation is based on WDS results measured at different spots on the sample as well as different samples in the same batch. Near the two ends of the series, the variation in substitution level is significantly smaller. The Co concentrations that are used to denote each batch of sample in the following text are the averaged values of measured concentrations.

Figure 2 shows the temperature-dependent resistivity data of Yb(Fe$_{1-x}$Co$_x$)$_2$Zn$_{20}$ on semilog plots. Figure 2(a) shows data closer to the pure YbFe$_2$Zn$_{20}$ side. At $x = 0$, the resistivity of YbFe$_2$Zn$_{20}$ shows a broad shoulder at ~40 K, after which it goes into a Kondo coherence. At low temperature, YbFe$_2$Zn$_{20}$ manifests a T^2 temperature dependence with the coefficient of T^2 resistivity, $A = 0.054$ $\mu\Omega$ cm/K^2 [6]. As the Co concentration increases, the resistivity value at 300 K increases, most likely resulting from increasing amount of scattering due to chemical disorder (i.e., Fe/Co). In addition, the temperature at which resistivity starts to decrease, after the low-temperature shoulder or local maximum, gradually shifts to lower temperatures, indicating a lowering of the Kondo coherence temperature. At $x = 0.064$, the low-temperature resistivity still follows a T^2 behavior with $A = 0.113$ $\mu\Omega$ cm/K^2. This value doubles the value for YbFe$_2$Zn$_{20}$ ($x = 0$). The A coefficient keeps increasing with Co concentration: ~0.173 $\mu\Omega$ cm/K^2 for $x = 0.129$ and ~0.197 $\mu\Omega$ cm/K^2 for $x = 0.170$. At $x = 0.375$, the low-temperature resistivity does not show a decrease and seems to saturate down to 500 mK. As x increases from zero to 0.375, Yb(Fe$_{1-x}$Co$_x$)$_2$Zn$_{20}$ evolves from a system with a clear Fermi-liquid signature in transport to one that does not.

Figure 2(b) shows resistivity data in the middle of the substitution range ($0.375 \leqslant x \leqslant 0.875$). None of the data shown have a clear signature of a resistivity drop that would be associated with a Kondo coherence. For $x = 0.628$ (blue star) and 0.719 (green dotted circle), the low-temperature resistivity data show a minor decrease which is followed by a secondary increase at a lower temperature. This is reminiscent of what
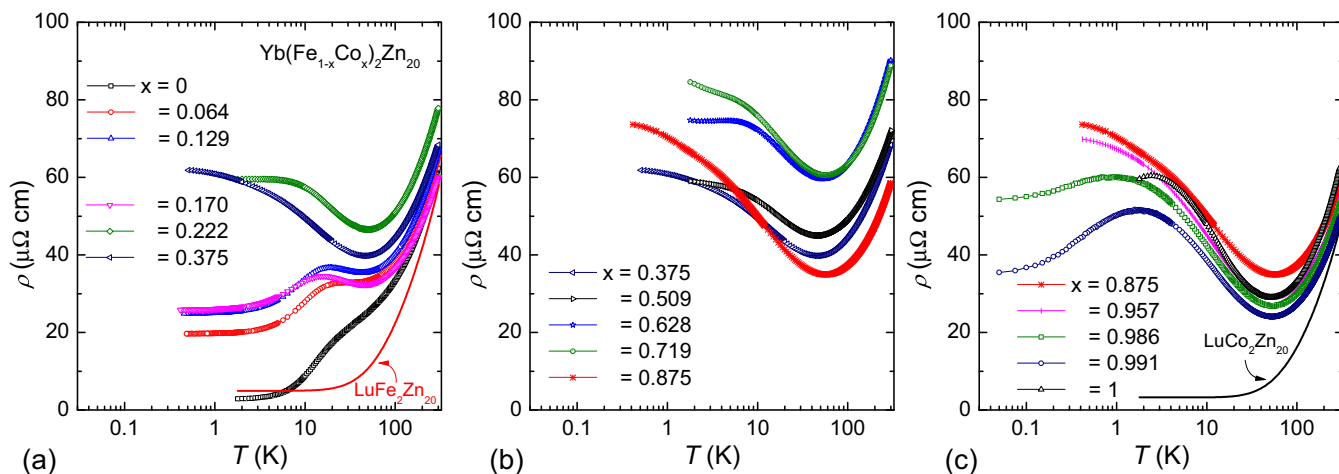

FIG. 2. Zero-field temperature-dependent resistivity of Yb(Fe$_{1-x}$Co$_x$)$_2$Zn$_{20}$ for a selection of Co concentrations on semilog plots. Resistivities of nonmagnetic LuFe$_2$Zn$_{20}$ and LuCo$_2$Zn$_{20}$ are also shown for comparison.
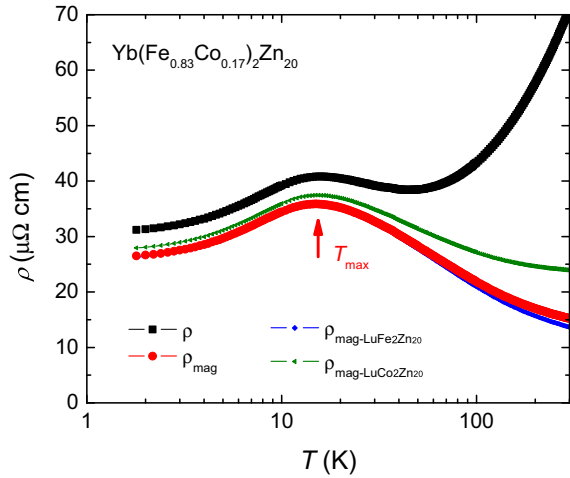
FIG. 3. Temperature-dependent resistivity for Yb(Fe$_{0.83}$Co$_{0.17}$)$_2$Zn$_{20}$ on a semilog plot. Black squares show the total resistivity. Red circles show the magnetic part of the resistivity. Blue diamonds and green triangles represent the magnetic part of resistivity by subtracting the resistivity of pure LuFe$_2$Zn$_{20}$ or LuCo$_2$Zn$_{20}$ (see text). Arrows indicate criteria for determining T_{max} from the ρ_{mag} data.

one would expect from a CEF feature when lowering the temperature depopulates the CEF levels and thus change the degeneracy participating in the Kondo effect [25]. However, it is unclear at this point if a coherence might be reached for these substitution levels for temperatures below 500 mK.

Figure 2(c) presents data close to the pure YbCo$_2$Zn$_{20}$ side ($0.875 \leqslant x \leqslant 1$). Black hollow triangles show the resistivity data for pure YbCo$_2$Zn$_{20}$ which are consistent with the previously reported results [6]. The resistivity increases with decreasing temperature below ~50 K, indicative of a Kondo effect. The drop of resistivity below 2 K is an indication of Kondo coherence. With a small amount of substitution of Fe for Co, shown by the blue hollow circles ($x = 0.991$)

and green hollow squares ($x = 0.986$), the temperature at which resistivity starts to drop decreases. With further Fe substitution, the Kondo coherence signature in resistivity could not be observed down to 500 mK as illustrated by purple bar ($x = 0.957$) and red star data ($x = 0.875$). Since the coherence temperature of YbCo$_2$Zn$_{20}$ is much lower than that for YbFe$_2$Zn$_{20}$, it takes less Fe substitution to suppress the coherence temperature of YbCo$_2$Zn$_{20}$ to below 500 mK.

Figure 3 illustrates the criteria that were used to infer characteristic temperatures for the Yb(Fe$_{1-x}$Co$_x$)$_2$Zn$_{20}$ compounds from the resistivity data. The magnetic part of resistivity was estimated by subtracting a combination of the resistivity for the nonmagnetic LuFe$_2$Zn$_{20}$ and LuCo$_2$Zn$_{20}$ with the same Fe/Co ratio. For example, in Fig. 3, the non-magnetic part of the resistivity data for Yb(Fe$_{0.83}$Co$_{0.17}$)$_2$Zn$_{20}$ was estimated as $0.83\rho_{LuFe_2Zn_{20}} + 0.17\rho_{LuCo_2Zn_{20}}$. Note, the estimated nonmagnetic part of the resistivity does not take into account the disorder scattering introduced by Fe/Co substitution, which will result in an additional temperature-independent residual resistivity. The band-filling effect is also omitted, which may give rise to a slightly different temperature dependence as compared to the current, linearly interpolated, resistivity values. The temperature of the maximum in ρ_{mag} was tracked as T_{max}. For comparison, the magnetic part of the resistivity estimated by subtracting the resistivity of pure LuFe$_2$Zn$_{20}$ (blue diamonds) and LuCo$_2$Zn$_{20}$ (green triangles) as well as the resistivity of Yb(Fe$_{0.83}$Co$_{0.17}$)$_2$Zn$_{20}$ (black squares) are also shown in Fig. 3. The temperatures of the maximum in all these data sets are similar and consistent. In the absence of low-temperature data for nonmagnetic subtraction below 1.8 K, the total resistivity data were then used to extract characteristic temperatures.

The temperature-dependent magnetic specific heat data for Yb(Fe$_{1-x}$Co$_x$)$_2$Zn$_{20}$ are shown in Fig. 4. Similar to the magnetic part of the resistivity, the specific heats of LuCo$_2$Zn$_{20}$ and LuFe$_2$Zn$_{20}$ were used to perform nonmagnetic background subtraction. Quantitatively, subtracting LuFe$_2$Zn$_{20}$ or

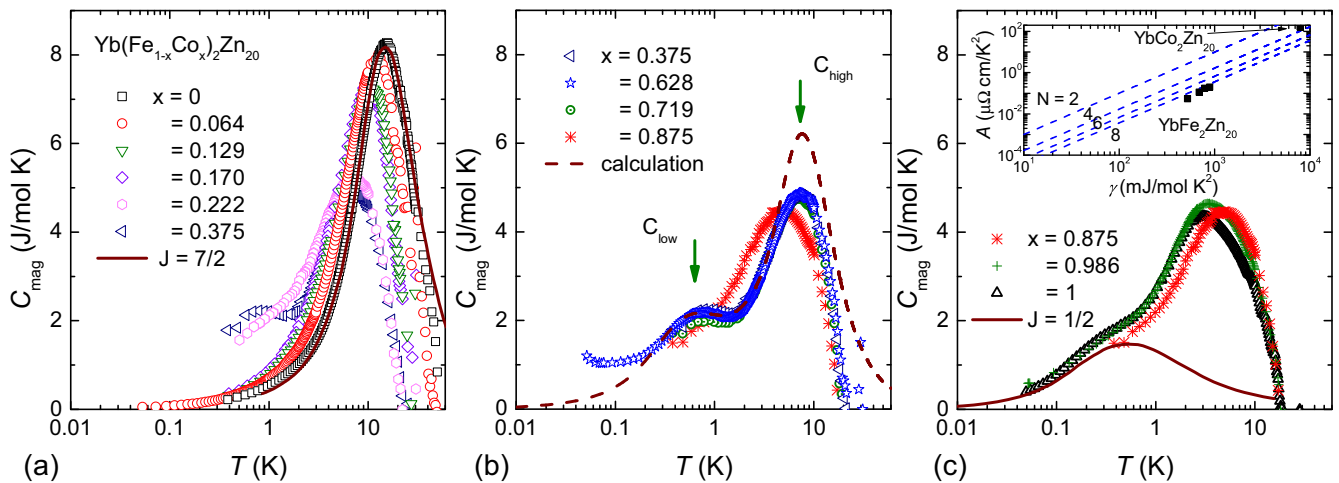

FIG. 4. Temperature-dependent magnetic specific heat of Yb(Fe$_{1-x}$Co$_x$)$_2$Zn$_{20}$ for a variety of Co concentrations. Solid lines in (a) and (c) represent magnetic specific heat of the Coqblin-Schrieffer model for $J = 7/2$ and $1/2$ [26,28]. The brown dashed line in (b) represents calculated magnetic specific heat based on a model proposed in Ref. [21] (see text). Green arrows indicate the criteria for determining C$_{high}$ and C$_{low}$. Inset in (c) is a generalized Kadowaki-Woods plot with N denoting the degeneracy that is responsible for the Kondo effect [29] and data points representing Yb(Fe$_{1-x}$Co$_x$)$_2$Zn$_{20}$ ($x = 0$, 0.064, 0.129, 0.170 and 1).

LuCo$_2$Zn$_{20}$ only results in a $\lesssim 2\%$ difference in the magnetic specific heat value and a $\lesssim 5\%$ change in characteristic temperature values. Therefore, for all the doped samples, a consistent nonmagnetic background specific heat of LuCo$_2$Zn$_{20}$ was subtracted.

The magnetic specific heat of YbFe$_2$Zn$_{20}$ [black squares in Fig. 4(a)] can be well explained by a $N = 8$ Kondo resonance as shown by the brown solid line [26]. With Co substitution, the Kondo resonance peak moves towards lower temperature accompanied by a decrease in maximum value. At $x = 0.064$, the electronic specific heat, γ, increases from 520 mJ/mol K^2 for YbFe$_2$Zn$_{20}$ [6] to 690 mJ/mol K^2. With more Co substitution, γ increases to ~ 790 mJ/mol K^2 for $x = 0.129$ and ~ 890 mJ/mol K^2 for $x = 0.170$. Together with the increase in the coefficient of T^2 resistivity, the positions of Yb(Fe$_{1-x}$Co$_x$)$_2$Zn$_{20}$ ($x = 0.064$, 0.129, and 0.170) on the generalized Kadowaki-Woods plot gradually move toward the YbCo$_2$Zn$_{20}$ side [6] as shown in the inset of Fig. 4(c). As Co substitution increases further, the single peak in YbFe$_2$Zn$_{20}$ gradually evolves to two maxima, as a result of competing energy scale of CEF splitting and the Kondo effect [27].

In between $0.375 \lesssim x \lesssim 0.719$, the magnetic specific heat data show very similar behavior. We keep track of the two maxima temperatures as C$_{high}$ (maximum that locates at a higher temperature) and C$_{low}$ (maximum that locates at a lower temperature) [Fig. 4(b)]. For $x = 0.628$, the specific heat was measured down to 50 mK. An upturn at below 100 mK was observed and will be discussed later. With more Co substitution, C$_{high}$ starts to move towards lower temperature.

Figure 4(c) shows magnetic specific heat data close to the pure YbCo$_2$Zn$_{20}$ side. From a generalized Kadowaki-Woods plot, the degeneracy that is responsible for Kondo coherence for YbCo$_2$Zn$_{20}$ is in between 2 and 4. The specific heat can be tentatively understood with a spin-1/2 Kondo resonance with additional contribution from higher-temperature Schottky peak features due to CEF splitting [20,21]. The brown solid line presents the magnetic specific heat due to a spin-1/2 Kondo resonance [26]. It captures, for the most part, the low-temperature part of the measured data (black triangles), with differences at higher temperatures coming from CEF effects, suggesting a doublet CEF ground state. With addition of Fe, the high-temperature maximum moves towards higher temperature, indicating a small increase of CEF splitting. In addition, the specific heat data exhibit a slight increase (for example, $x = 0.986$) at the base temperature, which may eventually evolve to the upturn seen for $x = 0.628$.

IV. DISCUSSION

Summarizing resistive and specific heat features presented above, we can plot characteristic temperatures of Yb(Fe$_{1-x}$Co$_x$)$_2$Zn$_{20}$ as a function of Co concentration, x. In Fig. 5, the green diamonds and cyan triangles represent characteristic temperatures inferred from specific heat data and black circles were inferred from resistivity measurements. At a gross level, the phase diagram can be divided into three regions. Two regions are on the pure YbFe$_2$Zn$_{20}$ or YbCo$_2$Zn$_{20}$ sides where the original Kondo lattice characteristic temperatures
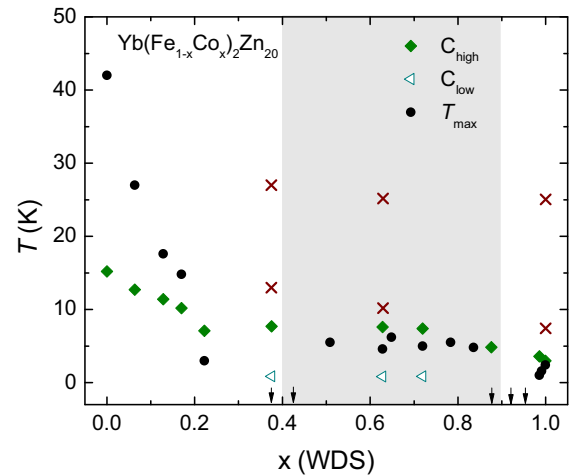

FIG. 5. Characteristic temperatures as a function of Co concentration in Yb(Fe$_{1-x}$Co$_x$)$_2$Zn$_{20}$. Green solid diamonds and cyan triangles represent specific heat maxima temperatures at high temperature and low temperature, respectively. Black circles represent T_{max} values extracted from resistivity data as illustrated in Fig. 3. Arrows at the bottom indicate samples that were measured resistively but showed no T_{max} down to 2 K ($x = 0.426$, 0.921) or 500 mK ($x = 0.375$, 0.875, 0.957). Brown crosses indicate the estimated energy of excited CEF levels for $x = 0.375$, 0.628, and 1. The gray shaded area separates the phase diagram into three regions as described in the text.

gradually evolve with Fe/Co substitution. The third region is in the middle where all feature temperatures are relatively similar and do not significantly change or evolve with x. The boundaries between these three regions are not sharply defined, partly due to a substitution variation, and partly due to the limitation of temperature range in measurements. On the YbFe$_2$Zn$_{20}$ side, the boundary may be located in between $x \sim 0.2$ and 0.4, and on the YbCo$_2$Zn$_{20}$ side the boundary may be around $x = 0.9$–0.95.

We first look at the two regions close to the pure YbFe$_2$Zn$_{20}$ and YbCo$_2$Zn$_{20}$ sides. The crossover from a high-temperature single-ion regime to a low-temperature coherent regime can usually be seen and inferred from temperature-dependent resistivity measurements [30,31]. In the coherent regime, the resistivity drops at low temperature, becoming a heavy Fermi-liquid state. Both YbFe$_2$Zn$_{20}$ and YbCo$_2$Zn$_{20}$ have a heavy Fermi liquid ground state down to 50 mK as evidenced by linear specific heat and a T^2 dependence in resistivity [5,6]. On the YbFe$_2$Zn$_{20}$ side, Co substitution suppresses T_{max} at roughly 1.8 K/%Co. At $x = 0.222$, the T_{max} is suppressed to 3 K. With more Co substitution, T_{max} was suppressed below the base temperature of measurements. A similar situation happens on the YbCo$_2$Zn$_{20}$ side. T_{max} is suppressed upon Fe substitution at roughly 1 K/%Fe. Given a much smaller, initial T_{max} value to start with, the trackable features quickly disappear to below 50 mK.

Magnetoresistance is sometimes used to probe the Kondo state at low temperature as well [32]. The single-ion Kondo regime has been theoretically calculated to show a negative magnetoresistance [33]. In the coherent regime, the compound is essentially a heavy Pauli-paramagnetic metal. Magnetoresistance therefore is most commonly positive. The
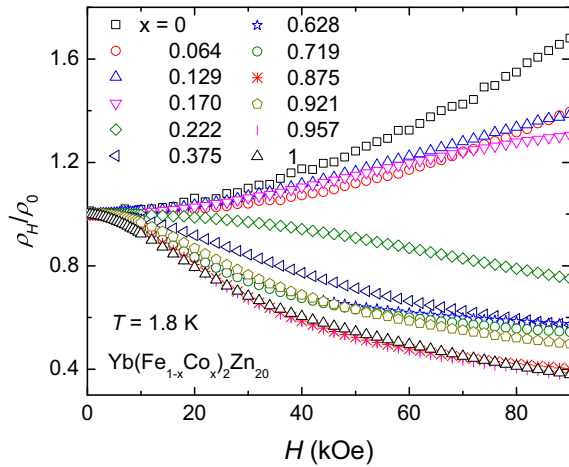
FIG. 6. Magnetoresistance of Yb(Fe$_{1-x}$Co$_x$)$_2$Zn$_{20}$ measured at 1.8 K up to 90 kOe.

magnetoresistance for YbFe$_2$Zn$_{20}$ is positive at 1.8 K, which is consistent with a coherent state (Fig. 6). For YbCo$_2$Zn$_{20}$, prior to the metamagnetic transition, the magnetoresistance is also positive below 0.1 K whereas it shows negative magnetoresistance above 3 K [19,34].

Magnetoresistance data are shown for various Co concentrations at 1.8 K in Fig. 6. Positive magnetoresistances for Co concentrations $x \lesssim 0.170$ suggest a coherence at 1.8 K. Other members ($x \geqslant 0.222$) show negative magnetoresistances that suggest a single-ion state. Assuming that the T_{max} is commensurate with coherence temperature, together with the magnetoresistance data, the coherence is suppressed on both ends of the phase diagram (Fig. 5). In the middle of the substitution range, however, no clear indication of coherence could be determined at 1.8 K.

Specific heat features close to the pure YbFe$_2$Zn$_{20}$ and YbCo$_2$Zn$_{20}$ sides evolve gradually with chemical substitution. On the YbFe$_2$Zn$_{20}$ side, with Co substitution, C$_{high}$ moves to lower temperature, indicating a lowering of Kondo temperature [26]. On the pure YbCo$_2$Zn$_{20}$ side, where the Kondo temperature is smaller than the CEF splitting, with Fe substitution, C$_{high}$ moves towards higher temperature, indicating a slight increase of CEF splitting.

The Kondo coherence feature in specific heat is much more subtle and under debate. Various models have proposed a decrease of density of states at the Fermi energy due the formation of coherence [35–38]. Experimentally, this decrease of density of states was used to explain the low-temperature drop in C/T (or γ) in different systems, for example, in CeAl$_3$ [39,40], CuCu$_6$ [41], CeNi$_2$Ge$_2$ [42], and CeCu$_2$Si$_2$ [40]. However, a feature associated with coherence in specific heat is not always so apparent and is commonly missing, for example, in YbNi$_2$B$_2$C [43], YbCuAl [44], CeCoGe$_2$ [45], YbAgCu$_4$ [46,47], and CeNi$_9$Si$_4$ [48]. A single-ion model based on a Coqblin-Schrieffer analysis [26,28] seems to describe these Kondo lattice systems very well, even in the coherent regime. For YbTM_2Zn$_{20}$, despite the fact that coherence emerges in resistivity at low temperature, specific heat can be well captured by single-ion Kondo effect [6].

Close to pure YbFe$_2$Zn$_{20}$ and YbCo$_2$Zn$_{20}$, it is shown above that upon Fe/Co substitution the coherence temperatures on both sides are suppressed. The suppression of coherence is commonly achieved by substituting the moment-bearing ions with non-moment-bearing ions [49]. In the case of Yb(Fe$_{1-x}$Co$_x$)$_2$Zn$_{20}$, moment-bearing Yb sites are always fully occupied and ordered. Substituting Fe/Co, however, will inevitably bring in chemical disorder as well as a change in band filling. As a consequence of chemical disorder, the decrease in mean-free path of the conduction electrons, as can be represented by the increase of residual resistivity, may lead to a suppression of Kondo coherence temperature [50]. This is sometimes also seen in systems with artificially created defects with irradiation [51]. Theoretically, it is proposed that disorder on the moment-bearing site (f site) affects Kondo coherence more efficiently than disorder on the conduction-electron sites. To produce the same suppression of Kondo coherence temperature, energetically, f-sites disorder needs to be equivalent to T_K whereas conduction-electron sites need to be comparable to the bandwidth of the conduction band, which is more difficult [52]. However, with a change of band filling due to Fe/Co substitution, disorder in the conduction-electron sites could affect Kondo coherence in these Yb(Fe$_{1-x}$Co$_x$)$_2$Zn$_{20}$ compounds.

The change in band filling due to Fe/Co substitution, on one hand, could be part of the disorder in conduction electrons in the aforementioned theoretical model. On the other hand, it may lead to a change in the ratio of Kondo coherence temperature over Kondo temperature, T_{coh}/T_K [53]. At half filling, it is proposed that T_{coh} is larger than T_K. Away from half filling, T_{coh} drops quickly below T_K [53]. It is possible that with changing band filling, T_{coh} decreases from both the YbFe$_2$Zn$_{20}$ and YbCo$_2$Zn$_{20}$ sides, which leaves a clear single-ion Kondo effect with features associated with CEF population whereas showing no coherence or a very low coherence temperature. Such an extended range of low T_{coh} is observed in the middle region of the phase diagram. A change in band filling may be inferred from the density of states at Fermi energy. It is worth noting that the density of states for YFe$_2$Zn$_{20}$ experiences a quick drop upon adding Co and stays relatively constant above 20% Co substitution [2]. This is very similar to the suppression of T_{max} close to the YbFe$_2$Zn$_{20}$ side. Close to the YCo$_2$Zn$_{20}$ side, though, there is not enough data density to make similar comparison to YbCo$_2$Zn$_{20}$.

We now move onto the middle region of the phase diagram shown in Fig. 5. Whereas there are clear changes of characteristic temperatures as the sample departs from perfect chemical order, in the middle region, for $0.4 \lesssim x \lesssim 0.9$, characteristic temperatures stay fairly constant. It is worth noting though, as shown in Fig. 1, the variation in concentration across a sample in this middle region may make the data blurred and offer only more qualitative information rather than quantitative. For a comparison of physical properties, despite the fact that the substitution variation is large in the middle region, the similarity between different compounds is still valid since the span of concentrations is larger than the variation. The sample sizes were large enough to represent the mean substitution levels that are presented here.

In a single-ion Kondo picture, different local-moment degeneracy can give rise to unique features in

thermodynamic and transport properties [25,28,54]. In the presence of crystalline electric field, features can be observed in temperature-dependent transport measurements, exhibited as broad maxima in resistivity, for example, in CeAl$_2$ [55], CeCu$_2$Si$_2$ [56], CePdIn [57], and CeZn$_{11}$ [58]. This was observed for several members of Yb(Fe$_{1-x}$Co$_x$)$_2$Zn$_{20}$ series, in the middle substitution range, for example, $x = 0.628$ and 0.719. However, the CEF feature is not as clear as systems mentioned above. If the CEF levels are not well separated, given a certain combination of density of states and Kondo coupling, these broad maxima can be hard to observe [25]. In the case of YbTM_2Zn$_{20}$, the CEF splitting is indeed small and may cause the CEF feature to be difficult to observe. Impurity scattering can also lead to a smear of Kondo CEF features. In YbNi$_2$B$_2$C, the improved sample quality after annealing dramatically changed the temperature-dependent transport properties. This can be attributed to a distribution of Kondo temperature in a nonideal lattice with local defects and strain [59]. In Yb(Fe$_{1-x}$Co$_x$)$_2$Zn$_{20}$, the substitution variation in the sample may cause such disorders even though transition metal is not in the direct neighborhood of the Yb ions.

To understand what happens in the middle of the substitution range in Yb(Fe$_{1-x}$Co$_x$)$_2$Zn$_{20}$, more insights can be obtained from the specific heat data. In the presence of crystal fields, the temperature dependence of magnetic specific heat in Kondo systems is complicated. An arbitrary CEF splitting has only been recently studied numerically for Ce-based compounds [27]. For Yb, more degeneracy, and levels, are involved. A quantitative interpretation of the temperature-dependent specific heat can be approached by combining a resonance model solution together with a CEF Schottky-like contribution [21]. In a cubic symmetry, Yb will be split into two doublets and a quartet. Assuming the quartet is at higher temperature, the temperature-dependent specific heat can be written as [21]

$$C_{\text{mag}} = C_{2d} - \frac{1}{k_B T^2}\left[\frac{\Delta^2 e^{-\Delta/k_B T}}{(1 + e^{-\Delta/k_B T})^2}\right] + C_s \qquad (1)$$

in which

$$C_{2d} = -\frac{k_B}{2(\pi k_B T)^2}\text{Re}\sum_{j=0}^{1}\left\{(\Gamma_j + i\Delta_j)^2\left[4\psi'\left(\frac{\Gamma_j + i\Delta_j}{\pi k_B T}\right)\right.\right.$$
$$\left.\left. - \psi'\left(\frac{\Gamma_j + i\Delta_j}{2\pi k_B T}\right)\right]\right\} + \frac{\Gamma_0 + \Gamma_1}{\pi T}, \qquad (2)$$

$$C_s = \frac{1}{k_B T^2}[(\Delta_1)^2 e^{-\Delta_1/k_B T} + 2(\Delta_2)^2 e^{-\Delta_2/k_B T}$$
$$+ 2(\Delta_2 - \Delta_1)^2 e^{-(\Delta_1+\Delta_2)/k_B T}](1 + e^{-\Delta_1/k_B T}$$
$$+ 2e^{-\Delta_2/k_B T})^{-2}. \qquad (3)$$

Here, C$_{2d}$ is the Kondo resonance contribution from the lower-lying two doublets. Γ_j represents the half width at half maximum of the spectral density for each crystal-field level. ψ' is the derivative of the digamma function and C$_s$ is the Schottky expression for a three level system. Δ_j represents the excited CEF energies. The second term in Eq. (1) accounts for the double counting of the Schottky contribution. Δ equals to Δ_1 ignoring complications of the ground-state doublet [21].

Δ_0 for the ground-state doublet is introduced to account for the resonance that is displaced away from the Fermi energy [21].

In Fig. 4(b), data for Yb(Fe$_{0.372}$Co$_{0.628}$)$_2$Zn$_{20}$ could be best fitted by the brown dashed line with parameters: $\Delta_0 = 1$ K, $\Delta_1 = 10$ K, $\Delta_2 = 25$ K, $\Gamma_0 = 0.87$ K, $\Gamma_1 = 4$ K. The low-temperature rise is omitted in the fit and will be discussed below. C$_{\text{low}}$ mainly comes from the Kondo effect for the ground-state doublet and C$_{\text{high}}$ largely comes from Schottky contribution due to CEF population. Therefore, the temperature of C$_{\text{high}}$ also reflects an upper limit of the total CEF splitting.

The calculated value qualitatively agrees with experimental data. Higher calculated values around 10 K might be due to an error caused by nonmagnetic background subtraction as illustrated by a negative value of C$_{\text{mag}}$ for $T > 20$ K. It could also be due to a lack of bandwidth information for the highest-lying quartet in the theoretical model [21]. Similar fit was also carried out for $x = 0.375$, which yields $\Delta_0 = 1.5$ K, $\Delta_1 = 13$ K, $\Delta_2 = 27$ K, $\Gamma_0 = 1$ K, and $\Gamma_1 = 5$ K. In general, the theoretical fits indicate that the two CEF levels are at around 10 and 25 K, which is close to what had been proposed for YbCo$_2$Zn$_{20}$ [20,21]. Thus at least to $x = 0.375$, as shown in Fig. 5, the CEF splitting does not change significantly from the pure YbCo$_2$Zn$_{20}$. In addition, since the temperature of C$_{\text{high}}$ sets an upper limit of the total CEF splitting, the total CEF splitting does not change much across the whole substitution range and may have increased slightly when approaching the YbFe$_2$Zn$_{20}$ side. In contrast, the CEF effect is more apparent for YbCo$_2$Zn$_{20}$. The difference in Kondo physics between YbFe$_2$Zn$_{20}$ and YbCo$_2$Zn$_{20}$ most likely originates from the difference in density of states as well as Kondo coupling strength.

Finally, as for the low-temperature rise in the specific heat of Yb(Fe$_{0.372}$Co$_{0.628}$)$_2$Zn$_{20}$, since there is no magnetic ordering or applied magnetic field, there should not be a nuclear Schottky anomaly due to Zeeman splitting of nuclear levels in specific heat measurement. However, the low-temperature upturn in the specific heat data observed below 100 mK could still come from a nuclear quadrupolar splitting of the ^{173}Yb nuclear moment [60]. Such quadrupole splitting for Yb in a cubic point symmetry may arise from the electric field gradient caused by chemical substitution induced distortion. Even though transition metal is not the first- nor the second-nearest neighbor of Yb, as substitution increases, the distortion to the original cubic symmetry increases. This is consistent with our observation that the low-temperature rise only emerges with chemical substitution and becomes more pronounced in the middle of the doping range. An alternative scenario is that the upturn is of a Kondo origin. However, that requires a decreasing CEF split energy upon substitution and a very small first excited CEF energy which was not observed in specific heat data. Instead, the C$_{\text{low}}$ feature stays unchanged for the majority of the substitution range which otherwise should also evolve and split.

We would also like to mention a similar doping series: CeNi$_9X_4$ ($X =$ Si, Ge) [61]. Changing from CeNi$_9$Ge$_4$ to CeNi$_9$Si$_4$, the Kondo temperature increases from ~4 to 70 K with ground-state CEF degeneracy changing from 4 for $X =$ Ge to 6 for $X =$ Si [61]. Upon doping, the coherence temperature drops quickly from both sides. In the middle of

the doping, specific heat shows continuous evolution from the high γ Ge side to the low γ Si side. Understanding the suppression of Kondo coherence in these two systems might offer useful insights into the formation of Kondo coherence.

V. CONCLUSIONS

In conclusion, we studied the evolution of Kondo effect in Yb(Fe$_{1-x}$Co$_x$)$_2$Zn$_{20}$ via resistivity and specific heat measurements. With Co substitution, the Kondo coherence temperature of YbFe$_2$Zn$_{20}$ decreases gradually with emerging features in specific heat that can be associated with CEF effect. On the YbCo$_2$Zn$_{20}$ side, the coherence temperature is also suppressed at the beginning of Fe substitution. In between, $0.4 \lesssim x \lesssim 0.9$, CEF features can be observed in both resistivity and specific heat data while showing no clear feature of coherence down to 500 mK. However, only qualitative information can be obtained in this middle region due to a large substitution level variation. Comparing all the experimental results, the CEF splitting stays roughly unchanged across the substitution series. The ground state of the compound evolves from a $N = 8$ coherent state for YbFe$_2$Zn$_{20}$ to a $N = 2$ coherent state in YbCo$_2$Zn$_{20}$. More measurements are needed to reveal the mechanism behind the suppression of coherence on the YbFe$_2$Zn$_{20}$ and YbCo$_2$Zn$_{20}$ side.

[1] T. Nasch, W. Jeitschko, and U. C. Rodewald, Z. Naturforsch. **52b**, 1023 (1997).

[2] S. Jia, S. L. Bud'ko, G. D. Samolyuk, and P. C. Canfield, Nat. Phys. **3**, 334 (2007).

[3] S. Jia, N. Ni, S. L. Bud'ko, and P. C. Canfield, Phys. Rev. B **76**, 184410 (2007).

[4] S. Jia, N. Ni, S. L. Bud'ko, and P. C. Canfield, Phys. Rev. B **80**, 104403 (2009).

[5] P. C. Canfield, S. Jia, E. Mun, S. L. Bud'ko, G. D. Samolyuk, and M. S. Torikachvili, Phys. B Condens. Matter **403**, 844 (2008).

[6] M. S. Torikachvili, S. Jia, E. D. Mun, S. T. Hannahs, R. C. Black, W. K. Neils, D. Martien, S. L. Bud'ko, and P. C. Canfield, Proc. Natl. Acad. Sci. USA **104**, 9960 (2007).

[7] E. D. Mun, S. Jia, S. L. Bud'ko, and P. C. Canfield, Phys. Rev. B **86**, 115110 (2012).

[8] Z. Fisk, P. C. Canfield, W. P. Beyermann, J. D. Thompson, M. F. Hundley, H. R. Ott, E. Felder, M. B. Maple, M. A. Lopez de la Torre, P. Visani, and C. L. Seaman, Phys. Rev. Lett. **67**, 3310 (1991).

[9] T. Tanaka and Y. Kubo, J. Phys. Soc. Jpn. **79**, 124710 (2010).

[10] Y. Saiga, K. Matsubayashi, T. Fujiwara, M. Kosaka, S. Katano, M. Hedo, T. Matsumoto, and Y. Uwatoko, J. Phys. Soc. Jpn. **77**, 053710 (2008).

[11] Y. Nakanishi, T. Kamiyama, K. Ito, M. Nakamura, Y. Saiga, M. Kosaka, Y. Uwatoko, and M. Yoshizawa, J. Phys.: Conf. Ser. **200**, 012142 (2010).

[12] S. K. Kim, M. S. Torikachvili, S. L. Bud'ko, and P. C. Canfield, Phys. Rev. B **88**, 045116 (2013).

[13] K. Matsubayashi, Y. Saiga, T. Matsumoto, and Y. Uwatoko, J. Phys.: Conf. Ser. **150**, 042117 (2009).

[14] K. Matsubayashi, Y. Saiga, T. Matsumoto, and Y. Uwatoko, J. Phys.: Conf. Ser. **200**, 012112 (2010).

[15] M. Cabrera-Baez, R. A. Ribeiro, and M. A. Avila, J. Phys.: Condens. Matter **28**, 375601 (2016).

[16] Y. Shimura, T. Sakakibara, S. Yoshiuchi, F. Honda, R. Settai, and Y. Ōnuki, J. Phys. Soc. Jpn. **80**, 073707 (2011).

[17] T. Takeuchi, M. Ohya, S. Yoshiuchi, M. Matsushita, F. Honda, R. Settai, and Y. Ōnuki, J. Phys.: Conf. Ser. **273**, 012059 (2011).

[18] Y. Shimura, T. Sakakibara, S. Yoshiuchi, F. Honda, R. Settai, and Y. Ōnuki, J. Phys.: Conf. Ser. **391**, 012066 (2012).

[19] F. Honda, Y. Taga, Y. Hirose, S. Yoshiuchi, Y. Tomooka, M. Ohya, J. Sakaguchi, T. Takeuchi, R. Settai, Y. Shimura, T. Sakakibara, I. Sheikin, T. Tanaka, Y. Kubo, and Y. Ōnuki, J. Phys. Soc. Jpn. **83**, 044703 (2014).

[20] T. Takeuchi, S. Yoshiuchi, M. Ohya, Y. Taga, Y. Hirose, K. Sugiyama, F. Honda, M. Hagiwara, K. Kindo, R. Settai, and Y. Ōnuki, J. Phys. Soc. Jpn. **80**, 114703 (2011).

[21] M. A. Romero, A. A. Aligia, J. G. Sereni, and G. Nieva, J. Phys.: Condens. Matter **26**, 025602 (2014).

[22] K. Kaneko, S. Yoshiuchi, T. Takeuchi, F. Honda, R. Settai, and Y. Ōnuki, J. Phys.: Conf. Ser. **391**, 012026 (2012).

[23] M. Ohya, M. Matsushita, S. Yoshiuchi, T. Takeuchi, F. Honda, R. Settai, T. Tanaka, Y. Kubo, and Y. Ōnuki, J. Phys. Soc. Jpn. **79**, 083601 (2010).

[24] P. C. Canfield, T. Kong, U. S. Kaluarachchi, and N. H. Jo, Philos. Mag. **96**, 84 (2016).

[25] B. Cornut and B. Coqblin, Phys. Rev. B **5**, 4541 (1972).

[26] V. T. Rajan, Phys. Rev. Lett. **51**, 308 (1983).

[27] H.-U. Desgranges, Phys. B: Condens. Matter **454**, 135 (2014).

[28] B. Coqblin and J. R. Schrieffer, Phys. Rev. **185**, 847 (1969).

[29] N. Tsujii, H. Kontani, and K. Yoshimura, Phys. Rev. Lett. **94**, 057201 (2005).

[30] D. L. Cox and N. Grewe, Z. Phys. B **71**, 321 (1988).

[31] E. Bauer, Adv. Phys. **40**, 417 (1991).

[32] M. C. Aronson, J. D. Thompson, J. L. Smith, Z. Fisk, and M. W. McElfresh, Phys. Rev. Lett. **63**, 2311 (1989).

[33] P. Schlottmann, Z. Phys. B **51**, 223 (1983).

[34] Y. Saiga, K. Matsubayashi, T. Fujiwara, T. Matsumoto, M. Kosaka, S. Katano, and Y. Uwatoko, J. Phys.: Conf. Ser. **150**, 042168 (2009).

[35] R. M. Martin, Phys. Rev. Lett. **48**, 362 (1982).

[36] N. Grewe, Solid State Commun. **50**, 19 (1984).

[37] C. Lacroix, J. Magn. Magn. Mater. **60**, 145 (1986).

[38] H. Kaga, H. Kubo, and T. Fujiwara, Phys. Rev. B **37**, 341 (1988).

[39] G. Brodale, R. Fisher, C. Lisse, N. Phillips, and A. Edelstein, J. Magn. Magn. Mater. **54–57**, 416 (1986).

[40] C. D. Bredl, S. Horn, F. Steglich, B. Lüthi, and R. M. Martin, Phys. Rev. Lett. **52**, 1982 (1984).

[41] T. Fujita, K. Satoh, Y. nuki, and T. Komatsubara, J. Magn. Magn. Mater. **47-48**, 66 (1985).

[42] G. Knopp, A. Loidl, R. Caspary, U. Gottwick, C. Bredl, H. Spille, F. Steglich, and A. Murani, J. Magn. Magn. Mater. **74**, 341 (1988).

[43] A. Yatskar, N. K. Budraa, W. P. Beyermann, P. C. Canfield, and S. L. Bud'ko, Phys. Rev. B **54**, R3772(R) (1996).

[44] P. Schlottmann, Phys. Rep. **181**, 1 (1989).

[45] E. D. Mun, B. K. Lee, Y. S. Kwon, and M. H. Jung, Phys. Rev. B **69**, 085113 (2004).

[46] C. Rossel, K. N. Yang, M. B. Maple, Z. Fisk, E. Zirngiebl, and J. D. Thompson, Phys. Rev. B **35**, 1914 (1987).

[47] M. Besnus, P. Haen, N. Hamdaoui, A. Herr, and A. Meyer, Phys. B Condens. Matter **163**, 571 (1990).

[48] H. Michor, S. Berger, M. El-Hagary, C. Paul, E. Bauer, G. Hilscher, P. Rogl, and G. Giester, Phys. Rev. B **67**, 224428 (2003).

[49] G. R. Stewart, Rev. Mod. Phys. **73**, 797 (2001).

[50] J. Paglione, T. A. Sayles, P.-C. Ho, J. R. Jeffries, and M. B. Maple, Nat. Phys. **3**, 703 (2007).

[51] G. Adrian and H. Adrian, J. Less-Common Met. **149**, 313 (1989).

[52] Z. Tešanović, Phys. Rev. B **34**, 5212 (1986).

[53] T. Pruschke, R. Bulla, and M. Jarrell, Phys. Rev. B **61**, 12799 (2000).

[54] A. K. Bhattacharjee and B. Coqblin, Phys. Rev. B **13**, 3441 (1976).

[55] M. Nicolas-Francillon, A. Percheron, J. Achard, O. Gorochov, B. Cornut, D. Jerome, and B. Coqblin, Solid State Commun. **11**, 845 (1972).

[56] H. Schneider, Z. Kletowski, F. Oster, and D. Wohlleben, Solid State Commun. **48**, 1093 (1983).

[57] H. Fujii, T. Takabatake, and Y. Andoh, J. Alloys Comput. **181**, 111 (1992).

[58] V. Taufour, H. Hodovanets, S. K. Kim, S. L. Bud'ko, and P. C. Canfield, Phys. Rev. B **88**, 195114 (2013).

[59] M. A. Avila, Y. Q. Wu, C. L. Condron, S. L. Bud'ko, M. Kramer, G. J. Miller, and P. C. Canfield, Phys. Rev. B **69**, 205107 (2004).

[60] A. Steppke, M. Brando, N. Oeschler, C. Krellner, C. Geibel, and F. Steglich, Phys. Status Solidi B **247**, 737 (2010).

[61] C. Gold, P. Gross, L. Peyker, G. Eickerling, G. G. Simeoni, O. Stockert, E. Kampert, F. Wolff-Fabris, H. Michor, and E.-W. Scheidt, J. Phys.: Condens. Matter **24**, 355601 (2012).